Vehicle System Dynamics
International Journal of Vehicle Mechanics and Mobility

ISSN: 0042-3114 (Print) 1744-5159 (Online) Journal homepage: www.tandfonline.com/journals/nvsd20

Design and validation of observer-based control for railway vehicles with driven independently rotating wheels: an experimental validation on a 1:5 scale test rig with coupled front and rear axis

Tobias Posielek

To cite this article: Tobias Posielek (03 Feb 2026): Design and validation of observer-based control for railway vehicles with driven independently rotating wheels: an experimental validation on a 1:5 scale test rig with coupled front and rear axis, Vehicle System Dynamics, DOI: 10.1080/00423114.2026.2621041

To link to this article: https://doi.org/10.1080/00423114.2026.2621041

VEHICLE SYSTEM DYNAMICS
https://doi.org/10.1080/00423114.2026.2621041

Design and validation of observer-based control for railway vehicles with driven independently rotating wheels: an experimental validation on a 1:5 scale test rig with coupled front and rear axis

Tobias Posielek

Institute of Vehicle Concepts, German Aerospace Center (DLR), Wessling, Germany

ABSTRACT

This paper presents a comprehensive study on the modelling, control, and observation of railway running gears with driven independently rotating wheels (DIRWs), focusing on both analytical derivations and experimental validation. A detailed system model is developed, capturing the coupling between front and rear axes, their different stability properties. A combined control and observer framework is proposed, with analytical formulations and closed-loop derivations provided. The control gains are tuned based on a decoupled axis assumption. Validation on the coupled system demonstrates that the dynamic behaviour remains consistent across configurations. This consistency is reflected in the eigenvalue comparisons, regardless of whether coupling or observation is included. Experimental tests conducted on a 1:5 scaled test rig confirm the effectiveness of the proposed approach. The system achieves satisfactory reference tracking within a few seconds, with steady-state deviations below 0.5 mm. Observations highlight small oscillations at wheel rotation frequencies, with the front axis exhibiting slightly higher deviations due to its inherent instability without control.

ARTICLE HISTORY
Received 14 July 2025
Revised 26 November 2025
Accepted 7 January 2026

1. Introduction

The performance of railway systems can be significantly enhanced by running gears with driven independently rotating wheels (DIRWs), which offer advantages such as improved centring on straight tracks, enhanced curve negotiation, and reduced noise and wheel-rail wear. However, these benefits rely on active control systems, which introduce complexity and demand rigorous validation compared to the long-established, passive track guidance systems used for nearly two centuries.

Nevertheless, there are already existing passive implementations of independently rotating wheel vehicles in operation. The most prominent example is the Talgo articulated train, which employs passive independently rotating wheelsets guided by a mechanical Watt linkage between adjacent car bodies [1]. This mechanism ensures that each running gear aligns

CONTACT Tobias Posielek ✉ tobias.posielek@dlr.de

approximately along the bisector of the carbody angles in curves, resulting in a stable radial positioning of the wheelsets and consequently smoother ride dynamics and reduced wear.

Modern railway applications, especially in high-speed and urban light rail contexts, present increasingly stringent requirements for stability and curving performance at higher speeds [2]. Meeting these demands necessitates the development of advanced control strategies and robust state estimation methods.

Within the German Aerospace Center's (DLR) 'Next Generation Train (NGT)' initiative [3], innovative running gear concepts featuring DIRWs have been explored. A key milestone of this initiative is the development of a 1:5 scaled prototype running gear, which serves as a highly controllable and cost-effective experimental platform for testing control and estimation strategies [3–6]. The associated roller rig is particularly distinctive, incorporating motorised actuation for each wheel and two independent wheel carriers with differing stability properties, making it an ideal testbed for evaluating the interaction of control and estimation techniques.

Designing effective control strategies for DIRWs involves addressing the complex, nonlinear nature of wheel-rail interactions. A straightforward approach for stabilisation, steering and guidance involves mimicking the behaviour of conventional wheelsets by regulating the differential angular velocity [7,8]. However, this approach sacrifices many of the unique advantages of DIRWs. The most important one is the ability to control the lateral displacement to a desired value. By doing so, it is possible to reduce wheel and rail wear, avoid localised running on a single spot and ensure more uniform load distribution across the wheel profile. Additionally, controlled lateral positioning can help mitigate hunting oscillations, improve curve negotiation, and maintain optimal contact conditions, further enhancing ride comfort and track longevity. Other approaches focus on stabilising the yaw angle [9] or directly controlling the lateral displacement to minimise wear and noise [10]. While simple controllers such as PID have been employed, their limitations in performance and robustness have driven research towards advanced techniques, including H_∞ control [11,12], model predictive control [13], and reinforcement learning [14].

In parallel, accurate state estimation poses an additional challenge. Direct measurement of lateral displacement using optical sensors is susceptible to interference from environmental factors like dirt, ballast, and weather [14]. As a result, indirect estimation using observers has gained attention. Observers use measurable variables, such as yaw angle and angular velocity, to estimate the lateral displacement. Prior studies have demonstrated the utility of Kalman filters [6] and simplified observer designs [15]. While these approaches have been applied successfully to individual axes in [16], they are yet to be tested when coupling between the front and rear axes exists.

This paper advances the state of the art by integrating a combined control and observer framework for both axes of the DLR 1:5 test rig, explicitly incorporating the coupling between them. To the authors' knowledge, this work presents the first demonstration of lateral reference trajectory tracking on a 1:5 DIRW test rig using only relative yaw angle and angular velocity measurements within an observer-based control framework. While previous research has made significant contributions in the context of whee–rail deflection estimation and related control tasks, these studies have typically relied on direct lateral displacement sensing, often based on optical measurements close to the rail, or have pursued alternative control objectives such as yaw angle or angular velocity regulation. These approaches, however, do not directly enable lateral reference trajectory tracking without lateral displacement measurements. The presented method therefore introduces a novel combination of sensing and control concepts that demonstrates the feasibility and robustness of coupled control and estimation for DIRWs and provides a foundation for further developments in this direction.

2. Notation

The i-th unit vector of $\mathbb{R}^n$ is defined by e_i. For an $n \in \mathbb{N}$ dimensional vector $x \in \mathbb{R}^n$ the i-th component is denoted by x_i and the components x_i to x_j where $i < j \leq n$ and $i, j \in \mathbb{N}$ are denoted by $x_{i:j} = [x_i \; \dots \; x_j]$. Similarly, for an $n \in \mathbb{N}$ times $m \in \mathbb{N}$ dimensional matrix $A \in \mathbb{R}^{n \times m}$, the component in the i-th row and j-th column is denoted by A_{ij} and the submatrix defined from the i_1 to the i_2 row and from the j_1 to the j_2 column is denoted by $A_{i_1:i_2, j_1:j_2}$. The variable 0 denotes the zero matrix of appropriate size. When necessary for clarification, 0_n is written to emphasise that it is the quadratic zero matrix of dimension $n \in \mathbb{N}$. Parameters of the front wheel carrier are denote by a subscript $\cdot_\mathrm{f}$ and parameters of the rear wheel carrier by a subscript $\cdot_\mathrm{r}$. A subscript $\cdot_m$ may denote either front or rear, i.e. $m \in \{\mathrm{f}, \mathrm{r}\}$. If explicitly stated, the subscript is omitted to enhance the readability.

3. Modelling

The development of a mathematical model that represents accurately the dynamics of the real system is fundsamental for the design of the lateral observer and controller. The derivation of this model and its parameter identification is presented in [17]. The dynamics of the system can be described by the state $x = [y_\mathrm{f}, \, \psi_\mathrm{f}, \, \dot{\psi}_\mathrm{f}, \, y_\mathrm{r}, \, \psi_\mathrm{r}, \, \dot{\psi}_\mathrm{r}]$ and the output $y^\mathrm{out} = [\psi_\mathrm{f}, \, \Delta\omega_\mathrm{f}, \, \psi_\mathrm{r}, \, \Delta\omega_\mathrm{r}]$ where $y_\mathrm{f}/y_\mathrm{r}$ is the lateral displacement of the front/rear wheel carrier, $\psi_\mathrm{f}/\psi_\mathrm{r}$,$\dot{\psi}_\mathrm{f}/\dot{\psi}_\mathrm{r}$ the relative yaw angle between front/rear wheel carrier and the vehicle frame and its derivative and $\Delta\omega_\mathrm{f}/\Delta\omega_\mathrm{r}$ the differential angular velocity between the left and right hand side wheel of the front/rear wheel carrier. The lateral displacement and relative yaw angle are illustrated in Figure 1. A more detailed version of this illustration covering also the transformation from the sensor measurements to the states is given in [17]. Note that $\psi_\mathrm{af}/\psi_\mathrm{ar}$ from Posielek [17] is denoted by $\psi_\mathrm{f}/\psi_\mathrm{r}$ in this work to enhance readability. The complete model of the system has the form

$$\dot{x} = Ax + Bu + x_\mathrm{off} \tag{1a}$$

$$y^\mathrm{out} = Cx + Du + y^\mathrm{out}_\mathrm{off} \tag{1b}$$

where the dynamics matrices are defined in Figure 2.

An overview of the parameters is given in Tables 1 and 2 and the derived parameters are $\bar{c}_{y,m} = \frac{(2r_0 \cos(\delta_{0,m})^3 - -2r_0 \cos(\delta_{0,m}) + b \cos(\delta_{0,m})^2 \sin(\delta_{0,m}))}{b \sin(\delta_{0,m})}$, $\Gamma_m = \frac{\tan(\delta_{0,m})}{\frac{b}{2} - r_0 \tan(\delta_{0,m})}$, $\omega_{0,m} = \sqrt{\frac{k_{c,m}}{J_{z,m}}}$, $D_m = \frac{k_{\mathrm{d},m}}{2J_{z,m}\omega_{0,m}}$ and $K_m = \frac{b}{r_0 J_{z,m} \omega_{0,m}^2} k_\tau$. The parameters are obtained using the methodology employed in [17], which leads to slightly different parameters of the front and rear axis. Notably, the parameters $\psi_\mathrm{off,f}$ and $\psi_\mathrm{off,r}$ are identical, because the influence of this parameter is in practice dominated by the influence of the hystersis as discussed in [17]. Additionally, the parameters $\bar{c}_{11,f}$ and $\bar{c}_{11,r}$ are identical because they are obtained based

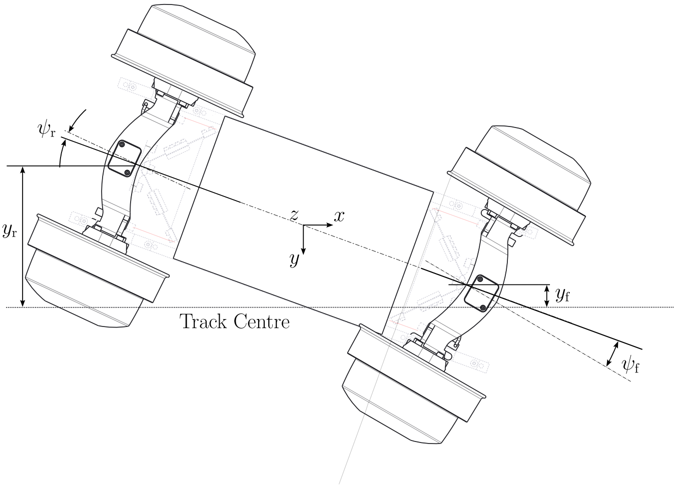

Figure 1. Illustration of the rail vehicle and its states. All quantities are highly exaggerated for clarity.

$$A = \begin{bmatrix} v\frac{\bar{c}_{y,\mathrm{f}}}{2l_{0,\mathrm{f}}} & v\bar{c}_{y,\mathrm{f}} & 0 & -v\frac{\bar{c}_{y,\mathrm{f}}}{2l_{0,\mathrm{f}}} & 0 & 0 \\ 0 & 0 & 1 & 0 & 0 & 0 \\ 0 & -\omega_{0,\mathrm{f}}^2 & -2D_\mathrm{f}\omega_{0,\mathrm{f}} & 0 & 0 & 0 \\ v\frac{\bar{c}_{y,\mathrm{r}}}{2l_{0,\mathrm{r}}} & 0 & 0 & -v\frac{\bar{c}_{y,\mathrm{r}}}{2l_{0,\mathrm{r}}} & v\bar{c}_{y,\mathrm{r}} & 0 \\ " & 0 & 0 & 0 & 0 & 1 \\ 0 & 0 & 0 & 0 & -\omega_{0,\mathrm{r}}^2 & -2D_\mathrm{f}\omega_{0,\mathrm{r}} \end{bmatrix} \quad B = \begin{bmatrix} 0 & 0 \\ 0 & 0 \\ K_\mathrm{f}\omega_{0,\mathrm{f}}^2 & 0 \\ 0 & 0 \\ 0 & 0 \\ 0 & K_\mathrm{r}\omega_{0,\mathrm{r}}^2 \end{bmatrix} \quad x_\mathrm{off} = \begin{bmatrix} v\frac{c_{\mathrm{y,f}}}{2l_{0,\mathrm{f}}}y_{\mathrm{off,f}} \\ 0 \\ \omega_{0,\mathrm{f}}^2\psi_{\mathrm{off,f}} \\ -v\frac{c_{\mathrm{y,r}}}{2l_{0,\mathrm{r}}}y_{\mathrm{off,r}} \\ 0 \\ \omega_{0,\mathrm{r}}^2\psi_{\mathrm{off,r}} \end{bmatrix}$$

$$C = \begin{bmatrix} 0 & 1 & 0 & 0 & 0 & 0 \\ \Gamma_\mathrm{f}\frac{b}{2r_0^2}v & 0 & \frac{b}{2r_0} & 0 & 0 & 0 \\ 0 & 0 & 0 & 0 & 1 & 0 \\ 0 & 0 & 0 & \Gamma_\mathrm{r}\frac{b}{2r_0^2}v & 0 & \frac{b}{2r_0} \end{bmatrix} \quad D = \begin{bmatrix} 0 & 0 \\ v\frac{k_\tau}{\bar{c}_{11,\mathrm{f}}r_0^2} & 0 \\ 0 & 0 \\ 0 & v\frac{k_\tau}{\bar{c}_{11,\mathrm{r}}r_0^2} \end{bmatrix} \quad y_\mathrm{off}^\mathrm{out} = \begin{bmatrix} 0 \\ \Delta\omega_{\mathrm{off,f}} \\ 0 \\ \Delta\omega_{\mathrm{off,r}} \end{bmatrix}$$

Figure 2. Dynamic Matrices.

Table 1. Parameters.

Notation	Description	Front $\cdot_\mathrm{f}$	Rear $\cdot_\mathrm{r}$
l_0	Distance wheel carrier and middle frame	0.283 m	0.280 m
δ_0	equivalent conicity	0.053 rad	0.050 rad
y_{off}	offset lateral displacement	0.002 m	−0.0006 m
$\bar{c}_{11}$	friction coefficient	$1.3 \cdot 10^5$ N rad^{-1}	$1.3 \cdot 10^5$ N rad^{-1}
ω_{off}	offset angular velocity	−0.002 rad s^{-1}	−0.009 rad s^{-1}
J_z	axle bridge inertia w.r.t yawing	0.43 kgm^2	0.36 kgm^2
k_c	equivalent stiffness	155.7 N m^{-1}	128.6 N m^{-1}
k_d	equivalent damping	73.5 N s m^{-1}	30.1 N s m^{-1}
ψ_{off}	offset yaw angle	$-1.4 \cdot 10^{-3}$ rad	$-1.4 \cdot 10^{-3}$ rad

on physical calculations in the spirit of Heckmann et al. [18] and their influence on the dynamics is almost negligible.

It is important to note that this model incorporates only the differential angular velocity, which is derived from a straightforward transformation between the left and right wheels. The mean angular velocity, however, is not included in the dynamics as it primarily governs

Table 2. Constants.

Notation	Description	Value
v	longitudinal velocity	$1\,\mathrm{m\,s^{-1}}$
r_0	wheel radius	$0.1\,\mathrm{m}$
b	track width	$0.3\,\mathrm{m}$
l_L	distance between laser sensors measuring lateral displacement	$0.1535\,\mathrm{m}$
b_0	nominal distance from laser sensors to metal plates	$0.065\,\mathrm{m}$
d_0	distance between laser sensors measuring yaw angle	$0.185\,\mathrm{m}$
k_τ	motor constant	$0.27\,\mathrm{N\,m\,A^{-1}}$
J_x	wheel inertia w.r.t rolling	$0.027\,\mathrm{kgm^2}$

traction control. While the control of the mean angular velocity represents a separate control task, it is not considered here, as the lateral dynamics are assumed to be independent of the mean angular velocity. The differential angular velocity itself is not modelled as a state but as an output obtained by the superposition of lateral displacement, yaw angle derivative and torque input. This is due to the fact that the angular velocity dynamics are extremely fast compared to the other dynamics as discussed in [17] and are therefore considered to be in steady state.

Roughly spoken, the dynamics represent that for each axis the applied differential torque induces a yaw angle which in turn induces a lateral displacement. A coupling between the two axes exists only in the lateral dynamics, and it is inversely proportional to the parameter l_0, which represents the distance between the wheel carrier and the middle frame. One key characteristic is that, for positive velocities, the front dynamics are unstable when $y_r = \psi_f = 0$, while the rear dynamics remain stable when $y_f = \psi_r = 0$. This distinction leads to significantly different control gain requirements for the front and rear axes [16]. Regarding the coupling, the time constant that defines these stability properties is also inversely proportional to the parameter l_0. For most railway vehicles, this parameter is relatively large, which is why the coupling and the differing stability characteristics are often neglected. However, in the case of the presented parameters for a scaled railway vehicle, these properties have a substantial impact and must therefore be accounted for in the controller and observer design. Additionally, note that the model is developed under the assumption of zero lateral slip, which reduces the lateral displacement dynamics from a second-order to a first-order differential equation. Overall, the model of the lateral dynamics have shown in [17] to be very consistent with the measurement results.

The two main factors lie in the yaw dynamics, as discussed in [17]. First, there is a hysteresis effect, which results in different outputs for the same constant inputs, depending on the history of previous inputs and states. In [17], this behaviour is modelled using a Bouc–Wen approach. However, it is not included in the proposed synthesis model (1) in order to preserve linearity. The hysteresis most likely originates from the spring connecting the carbody with the two wheel carriers. Secondly, and more critically, Posielek [17] shows that the damping parameter D varies significantly during a simple step response. This variation is complex and is most likely caused by the interaction between the wheel and rail. The damping variation appears to depend on several factors, including the input u and its derivative. Although this variation is not accounted for in the proposed model, it is considered during the design of the controller and observer to ensure that the closed-loop system remains stable across a wide range of damping parameters.

Not all states can be directly measured. While the yaw angles ψ_f and ψ_r can be measured using laser sensors or linear variable differential transformers, and the differential angular velocity can be obtained via encoders, lateral displacement is typically measured with 3D laser profilers [19]. However, these profilers are often affected by external factors such as dirt, swirling ballast, and weather conditions near the track bed, making them less reliable. Thus, an observer is required exploiting the dynamics (1) to obtain an estimation of y_m which can be used in the control.

For the system identification, control design as well as observer design it is beneficial to split the system into the system dynamics of the front and the rear dynamics. These are obtained to be in the form

$$\dot{x}_m = A_m x_m + B_m u_m + x_{\mathrm{off,m}} + W_m x_{\bar{m}} \tag{2a}$$

$$y_m^{\mathrm{out}} = C_m x_m + D_m u_m + y_{\mathrm{off,m}}^{\mathrm{out}} \tag{2b}$$

where the front or rear is denoted by $m \in \{\mathrm{f}, \mathrm{r}\}$ and the opposite side is denoted by $\bar{m}$. The front or rear state is defined by $x_m = [y_m, \ \psi_m, \ \dot{\psi}_m]$ and the output as $y_m^{\mathrm{out}} = [\psi_m, \ \Delta\omega_m]$. The structure of (2) is identical to the complete system (1) but for the fact that the states of the opposite side $x_{\bar{m}}$ are considered as disturbances acting via the disturbance matrix W_m on the system. The dynamics matrices and offsets are straightforwardly obtained from the original matrices by removing the appropriate rows and columns

$$A_{\mathrm{f}} = A_{1:3,1:3} \quad B_{\mathrm{f}} = B_{1:3,1} \quad W_{\mathrm{f}} = A_{1:3,4:6} \tag{3a}$$

$$C_{\mathrm{f}} = C_{1:2,1:3} \quad D_{\mathrm{f}} = D_{1:2,1} \tag{3b}$$

$$x_{\mathrm{off,f}} = x_{\mathrm{off},1:3} \quad y_{\mathrm{off,f}} = y_{\mathrm{off},1:2} \tag{3c}$$

$$A_{\mathrm{r}} = A_{4:6,4:6} \quad B_{\mathrm{r}} = B_{4:6,2} \quad W_{\mathrm{r}} = A_{4:6,1:3} \tag{3d}$$

$$C_{\mathrm{r}} = C_{3:4,4:6} \quad D_{\mathrm{r}} = D_{3:4,2} \tag{3e}$$

$$x_{\mathrm{off,r}} = x_{\mathrm{off},4:6} \quad y_{\mathrm{off,r}} = y_{\mathrm{off},3:4}. \tag{3f}$$

4. Control design

The almost decoupled nature of the front and rear wheel carrier suggests a separate design of control for front and rear wheel carriers. This has the advantage that the control task is reduced to a problem of smaller dimension and the two-wheel carrier can be analysed separately. Thus, in the remainder of this section, the index $\cdot_m$ is omitted for all variables and parameters in the system of Equation (4) in order to enhance the readability.

4.1. Cascaded PI-PD controller

The proposed control structure for both wheel carriers is a cascaded PI-PD controller as proposed in [16,17] and illustrated in Figure 3. The D part in the inner loop is used to induce a constant damping into the system and therefore reduce the influence of the varying damping discussed in the previous section. The integral part is used to have no steady state error which would despite a prefilter be introduced by the hysteresis neglected here in the modelling as discussed in [20]. Finally, the advantage of the cascaded structure is that the gains can be tuned in an iterative manner as discussed in [17].

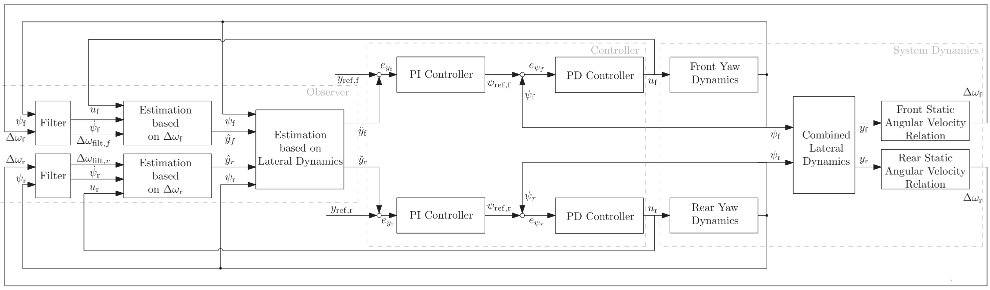

Figure 3. Block diagram combined observer and controller structure.

It is defined in a cascaded manner by

$$u = K_{P,\psi} e_\psi + K_{D,\psi} \hat{e}_{\dot\psi} \tag{4a}$$

$$e_\psi = \psi_{\text{ref}} - \psi \qquad \hat{e}_{\dot\psi} = \dot\psi_{\text{ref}} - \hat{\dot\psi} \tag{4b}$$

$$\dot x_{\text{diff}} = -\frac{1}{T_\psi} x_{\text{diff}} + \psi \qquad \hat{\dot\psi} = -\frac{1}{T_\psi^2} x_{\text{diff}} + \frac{1}{T_\psi}\psi \tag{4c}$$

$$\psi_{\text{ref}} = K_{P,y} e_y + K_{I,y} x_I \tag{4d}$$

$$e_y = y_{\text{ref}} - y \qquad \dot x_I = e_y \tag{4e}$$

where $K_{P,\psi}$, $K_{D,\psi}$, $K_{P,y}$, $K_{I,y}$, T_ψ are the tuning parameters of the control. The new state x_{diff} and estimation $\hat{\dot\psi}$ are a state space representation of the differentiator transfer function $\frac{s}{T_\psi s+1}$. Equivalently, the control law can be written in the form $u = -G[x_I, x, x_{\text{diff}}]^\top + u_{\text{off}}$ with

$$\begin{aligned}
G_{1:2} &= \left[K_{I,y}K_{P,\psi} \;\; K_{D,\psi}(K_{I,y} + s_m \tfrac{K_{P,y}\bar c_y v}{l_0}) - K_{P,y}K_{P,\psi}\right] \\
G_{3:5} &= \left[-K_{P,\psi} - K_{D,\psi}\left(\tfrac{1}{T_\psi} + K_{P,y}\bar c_y v\right) \quad 0 \quad \tfrac{K_{D,\psi}}{T_m^2}\right] \\
u_{\text{off}} &= K_{D,\psi}K_{P,y}\dot y_{\text{ref}} + K_{D,\psi}K_{I,y}y_{\text{ref}} - K_{P,\psi}K_{P,y}y_{\text{ref}}
\end{aligned} \tag{5}$$

where $s_f = 1$ and $s_r = -1$ shows the only structural difference between front and rear gain in the second component. Note that in (4) and (5) the subscript $\cdot_m$ is omitted at all states and parameters but s_m to improve clarity.

In this form it can be seen that the presented PI-PD control is equivalent to a full state feedback with additional integrator state. It is worth noting that due to the cascaded structure and the differentiator the control law u as in (5) is varying with the velocity v in the second and third component.

4.2. Closed loop

The description of the closed loop is vital in order to access the stability properties of the closed-loop system as used in Section 7. The closed loop for front and rear wheel carrier have the form $\dot x_m^{\text{cl}} = A_{\text{m}}^{\text{cl}} x_m^{\text{cl}} + W_{\text{m}}^{\text{cl}} x_{\bar m}^{\text{cl}} + x_{\text{off},m}^{\text{cl}}$ with $x_m^{\text{cl}} = [x_{I,m}, x_m, x_{\text{diff},m}]^\top$, $x_{\bar m}^{\text{cl}} =$

$[x_{\mathrm{I},\bar{m}}, x_{\bar{m}}, x_{\mathrm{diff},\bar{m}}]^\top$, $A_m^{\mathrm{cl}} = A_m^{\mathrm{o}} - B_m^{\mathrm{o}} G_m$, $W_m^{\mathrm{cl}} = \mathrm{diag}(0, W_m, 0)$ and

$$A_{\mathrm{m}}^{\mathrm{o}} = \begin{bmatrix} 0 & -e_1^\top & 0 \\ 0 & A_m & 0 \\ 0 & -e_2^\top & -\frac{1}{T_{\psi,m}} \end{bmatrix} \qquad B_{\mathrm{m}}^{\mathrm{o}} = \begin{bmatrix} 0 \\ B_m \\ 0 \end{bmatrix}$$

$$x_{\mathrm{off},m}^{\mathrm{cl}} = \begin{bmatrix} y_{\mathrm{ref}} & s_m \frac{\bar{c}_{y,m} v y_{\mathrm{off,m}}}{2 l_{0,\mathrm{f}}} & 0 & x_{\mathrm{off},m,4}^{\mathrm{cl}} & 0 \end{bmatrix}$$

$$\begin{aligned} x_{\mathrm{off},m,4}^{\mathrm{cl}} &= w_{0,m}^2 (\psi_{\mathrm{off},m} + K_m K_{\mathrm{D},\psi} K_{\mathrm{P},y} \dot{y}_{\mathrm{ref}} \\ &= + K_m K_{\mathrm{D},\psi} K_{\mathrm{I},y} y_{\mathrm{ref}} - K_m K_{\mathrm{P},y} K_{\mathrm{P},\psi} y_{\mathrm{ref}}) \end{aligned}$$

where e_1, e_2 denote the first and second unit vector of dimension three. Employing both controllers for the front and rear wheel carrier simultaneously leads to the closed-loop system $\dot{x}^{\mathrm{cl}} = A^{\mathrm{cl}} x^{\mathrm{cl}} + x_{\mathrm{off}}^{\mathrm{cl}}$ where

$$\begin{bmatrix} x_{\mathrm{off,f}}^{\mathrm{cl}} \\ x_{\mathrm{off,r}}^{\mathrm{cl}} \end{bmatrix}$$

This description of the closed loop is used in Section 6 to assess the stability of the proposed controller design.

5. Observer design

As discussed in Section 3 an observer is vital in order to obtain an estimate of the control variables y_f and y_r. It is noteworthy that the non-flatness of the wheels is responsible for the observability of the system, since the system is observable if and only if the equivalent conicity $\delta_{0,m}$ is not identical to zero.

5.1. Design

For the structure of the observer, the design in [15] is proposed. It has the main advantage that it relies only on a minimal amount of model information and has only a single tuning parameter for each axis. Similar to the control design in Section 4 it is sensible to design the observer for both wheel carriers independently. An overview about its structure can be seen in Figure 3.

As introduced in [15] the observer can be considered to be of two steps. The first uses the differential angular velocity dynamics to obtain a first estimate of the lateral displacement

$$\begin{aligned} \hat{y} &= -\frac{r_0}{v\Gamma_m} \dot{\psi}_{\mathrm{filt},m} + \frac{2r_0^2}{bv\Gamma_m} \Delta\omega_{\mathrm{filt},m} \\ &= -\frac{2}{b\bar{c}_{11,m}\Gamma_m} k_\tau u_m - \frac{2r_0^2}{\Gamma_m bv} \Delta\omega_{\mathrm{off},m}. \end{aligned} \tag{6}$$

where $\dot{\psi}_{\text{filt}}$ and $\Delta\omega_{\text{filt}}$ are low-passed filtered signals of the measured signals, i.e.

$$\Delta\dot{\omega}_{\text{filt},m} = -\frac{1}{T_{\Delta\omega,m}}\Delta\omega_{\text{filt},m} + \frac{1}{T_{\Delta\omega,m}}\Delta\omega_m \tag{7a}$$

$$\dot{x}_{\text{diff,O},m} = -\frac{1}{T_{\Delta\omega,m}}x_{\text{diff,O},m} + \psi_m \tag{7b}$$

$$\dot{\psi}_{\text{filt},m} = -\frac{1}{T^2_{\Delta\omega,m}}x_{\text{diff,O},m} + \frac{1}{T_{\Delta\omega,m}}\psi_m\,. \tag{7c}$$

Note that the estimation of $\dot{\psi}_m$ in Equations (7b) and (7c) is identical to the estimation in the controller (4c). However, it is beneficial to synchronise the time constant with (7a) to improve the estimate of the lateral displacement.

The second step uses the lateral dynamics to filter the estimate via

$$\dot{\check{y}}_m = s_m v\frac{\bar{c}_{y,m}}{2l_{0,m}}\check{y}_m + v\bar{c}_{y,m}\psi_m - s_m v\frac{\bar{c}_{y,\bar{m}}}{2l_{0,\bar{m}}}\check{y}_{\bar{m}} \tag{8}$$

$$= +v\frac{\bar{c}_{y,m}}{2l_{0,m}}y_{\text{off},m} + L_m(\hat{y}_m - \check{y}_m) \tag{9}$$

Compared to conventional methods like Luenberger observer or Kalman filters this observer does not estimate the complete state x but only the required control variable y_m.

5.2. Closed loop

In order to determine the closed loop dynamic, the estimation error $e_{y_m} = y_m - \check{y}_m$ is introduced. The overall closed loop state is defined by $z_m = [x^{\text{cl}}_m, e_{y_m}, \Delta\omega_{\text{filt},m}, x_{\text{diff,O},m}]$ with x^{cl}_m defined as in Section 4.2. The control introduced in Section 4 is adapted such that the real lateral displacement y_m is replaced by its estimate $\check{y}_m$ and can therefore be written as

$$u = -G_m[x^{\text{cl}}_{m,1}, \check{y}_m, x^{\text{cl}}_{m,3:5}]^\top + u_{\text{off}}. \tag{10}$$

The integrator state has slightly changed dynamics compared to (4e) due to using the estimate $\check{y}_m$ instead of y_m, i.e.

$$x_{\text{I,m}} = y_{\text{ref},m} - \check{y}_m = y_{\text{ref},m} - (e_2 - e_6)^\top z_m \tag{11}$$

where $e_2 \in \mathbb{R}^5$ and $e_6 \in \mathbb{R}^8$ are the unit vectors of appropriate dimensions. Defining $C^{\text{cl}}_m = [0, C_{m,2,:}, 0]$, $D^{\text{cl}}_m = D_{m,2,:}$ allows to write the angular velocity defined in (2b) as

$$\Delta\omega_m = ((C^{\text{cl}}_m - D^{\text{cl}}_m G_m)I_{5,8} + D^{\text{cl}}_m G_m e_2 e_6^\top)z + D^{\text{cl}}_m u_{\text{off}}. \tag{12}$$

The filtered yaw angle defined in Equation (7c) can be written as

$$\dot{\psi}_{\text{filt},m} = \left(\frac{1}{T_{\Delta\omega,m}}e_3^\top - \frac{1}{T^2_{\Delta\omega,m}}e_8^\top\right)z \tag{13}$$

and the estimate of the lateral displacement from Equation (6) can consequently be written as

$$\hat{y}_m = \left(\frac{2k_\tau G}{b\bar{c}_{11}\Gamma} I_{5,8} - \frac{r_0}{v_0 \Gamma T_{\Delta\omega}} e_3^\top - \frac{2k_\tau G e_2}{b\bar{c}_{11}\Gamma} e_6^\top + \frac{2r_0^2}{b v_0 \Gamma} e_7^\top + \frac{r_0}{v_0 \Gamma T_{\Delta\omega}^2} e_8^\top \right) z \\ - \frac{2k_\tau}{b\bar{c}_{11}\Gamma} u_{\text{off}} - \frac{2r_0^2}{\Gamma b v} \Delta\omega_{\text{off}} \tag{14}$$

where the subscript $\cdot_m$ is omitted on the right-hand side to enhance the readability.

This allows to define the observation error e_{y_m} as

$$\dot{e}_{y_m} = \bar{A}^{\text{cl}}_{6,1:5} z_{1:5} + \left(\bar{A}^{\text{cl}}_{6,6} e_6^\top - L \frac{2r_0^2}{b v_0 \Gamma} e_7^\top - L \frac{r_0}{v_0 \Gamma T_{\Delta\omega}^2} e_8^\top \right) z \\ - s_m v \frac{\bar{c}_{y,\bar{m}}}{2 l_{0,\bar{m}}} e_{y_{\bar{m}}} + L \frac{2k_\tau}{b\bar{c}_{11}\Gamma} u_{\text{off}} + L \frac{2r_0^2}{\Gamma b v} \Delta\omega_{\text{off}} \tag{15}$$

where

$$\bar{A}^{\text{cl}}_{\text{m},6,1:5} = -L_m \frac{2k_\tau G_m}{b\bar{c}_{11,m}\Gamma} I_{1:5,5} + L_m \frac{r_0}{v_0 \Gamma_m T_{\Delta\omega,m}} e_3^\top$$

$$\bar{A}^{\text{cl}}_{\text{m},6,6} = L_m \frac{2k_\tau G_m e_2}{b\bar{c}_{11,m}\Gamma} - L_m + s_m v \frac{\bar{c}_{y,m}}{2 l_{0,m}}$$

Combining the closed loop dynamics from Section 4.2, the estimation error dynamics (15) and the filtering dynamics (7) leads to the closed loop dynamics $\dot{z}_m = \bar{A}^{\text{cl}}_{\text{m}} z_m + \bar{W}^{\text{cl}}_m z_{\bar{m}} + z_{\text{off,m}}$ with

$$\bar{A}^{\text{cl}}_{\text{m}} = \begin{bmatrix} A^{\text{cl}} & e_1 + B^{\text{o}} G e_2 & 0 & 0 \\ \bar{A}^{\text{cl}}_{6,1:5} & \bar{A}^{\text{cl}}_{6,6} & -L\frac{2r_0^2}{b v_0 \Gamma} & -\frac{G r_0}{v_0 \Gamma T_{\Delta\omega}^2} \\ C^{\text{cl}} - D^{\text{cl}} G & D^{\text{cl}} G e_2 & -\frac{1}{T_{\Delta\omega}} & 0 \\ e_3^\top & 0 & 0 & -\frac{1}{T_{\Delta\omega}} \end{bmatrix}$$

$$\bar{W}^{\text{cl}}_m = \operatorname{diag}\left(0_5, -s_m v \frac{\bar{c}_{y,\bar{m}}}{2 l_{0,\bar{m}}}, 0_2 \right)$$

$$z_{\text{off,m}} = \begin{bmatrix} x^{\text{cl}}_{\text{off}} \\ G_m \left(\frac{2k_\tau}{b\bar{c}_{11,m}\Gamma} u_{\text{off}} + \frac{2r_0^2}{\Gamma_m b v} \Delta\omega_{\text{off}} \right) \\ D^{\text{cl}}_m u_{\text{off}} \\ 0 \end{bmatrix}$$

where the subscript $\cdot_m$ is omitted on the right hand side to enhance the readability.

When both controller and observers are employed the complete closed loop matrix has the form $\dot{z} = \bar{A}^{\text{cl}} z + z^{\text{cl}}_{\text{off}}$ where

$$\begin{bmatrix} z_{\text{off,f}} \\ z_{\text{off,r}} \end{bmatrix}$$

6. Control and observer gain tuning

We follow the gain-tuning methodology proposed in [16] which adopts a sequential approach, starting with the controller gains and followed by observer parameters. The resulting parameters are given in Table 3. The controller gains are tuned by progressively addressing the outer and inner loops, while ensuring robustness and stability under state and actuator constraints. For yaw dynamics, the proportional and derivative gains $K_{\mathrm{P},\psi}$ and $K_{\mathrm{D},\psi}$ are selected based on structural symmetry, system sample time, and noise characteristics, with the time constant T_{ψ} chosen to accurately approximate the derivative of ψ given the low noise levels and sampling rate. For lateral dynamics, the proportional and integral gains are designed to satisfy closed-loop eigenvalue requirements and ensure robustness, with $K_{\mathrm{I,y},m}$ directly taken from prior validated designs [16] to ensure steady-state performance and system stability.

Similarly, observer parameters $T_{\Delta\omega,m}$ and L_m are adjusted to balance filtering performance and asymptotic stability. These parameters ensure the slowest eigenvalue remains stable under the constraints of high-frequency noise in $\Delta\omega$, as discussed in [16].

To validate the stability of the closed-loop system, the eigenvalues are analysed and presented in Figure 4. The eigenvalues, as derived in Section 5.2, are evaluated under various configurations. First, the case without an observer is considered, where the lateral displacement is assumed to be directly measurable. Additionally, the eigenvalues of the decoupled system, where no coupling between the front and rear axes is assumed (i.e. $W_{\mathrm{f}}^{\mathrm{cl}} = W_{\mathrm{r}}^{\mathrm{cl}} = 0$), are examined. This scenario is particularly relevant as the gain design was based on this decoupled assumption. Furthermore, the eigenvalues of the complete system, including the observer as described in Section 5.2, are analysed. Both decoupled and coupled configurations are investigated to provide a comprehensive evaluation of the system's stability and design consistency. The results reveal that the fast eigenvalues are almost identical across all four configurations. In contrast, for the slow eigenvalues, differences in both the real and imaginary parts are observed. Nevertheless, all eigenvalues remain stable across all configurations. Notably, the decoupled observer configuration exhibits slower eigenvalues compared to the coupled observer configuration. In summary, the parameter tuning process, which is based on the decoupling assumption between the front and rear

Table 3. Tuned parameters.

	$K_{P,y,m}$	$K_{I,y,m}$	$K_{P,\psi,m}$	$K_{D,\psi,m}$	$T_{\psi,m}$	L_m	$T_{\Delta\omega,m}$
Front	12	3	50	5	0.005	3	0.07
Rear	3	3	50	5	0.005	3	0.07

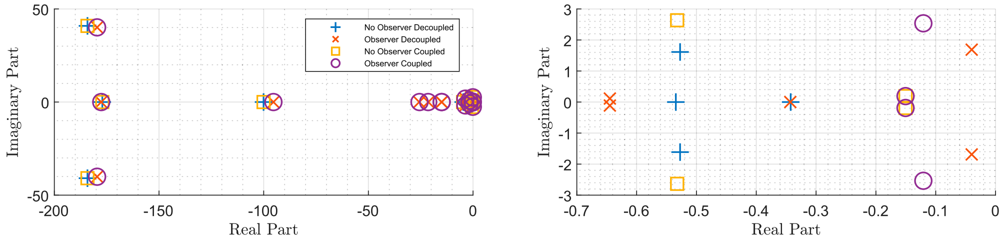

Figure 4. Eigenvalues of the closed loop.

axes, performs effectively. The resulting design not only ensures stability for the coupled system but also retains eigenvalues in a similar range across configurations.

7. Test rig

In this section, the observer and controller proposed in the previous sections are applied to the 1:5 test rig. First, details about the test rig and its setup are given. Then, the proposed control and observer combination is validated on the test rig by two scenarios in the same fashion as in [15–17]. First, the performance is evaluated by tracking three steps with different step heights. Secondly, the robustness is investigated by controlling the lateral distance to zero while adding external disturbances to the system.

7.1. Setup

A visual impression of the 1:5 test rig investigated throughout this paper can be found in Figure 5.

The running gear consists of four DIRWs, each independently driven by motors housed within the wheels. These motors are permanently-excited synchronous machines, each controlled by its own power converter, and provide based on the commanded input current u the required differential torque to steer the system.

Each pair of wheels is connected by an axle bridge, which is coupled to the running gear frame via a leaf spring guidance system that enables the yaw motion of the axle bridges. The running gear is mounted on two revolving rollers, simulating the longitudinal motion of the vehicle.

The test rig is equipped with several sensors for the control and monitoring of the DIRWs as displayed in Figure 6. At (1) two laser sensors are mounted on the roller rig frame which measure the distance to two metal plates at the front and rear ultimately leading to the measurements y_f/y_r. Additionally, at (2), four laser sensors are mounted at the front left, front right, rear left and rear right on the running gear frame, measuring the distances

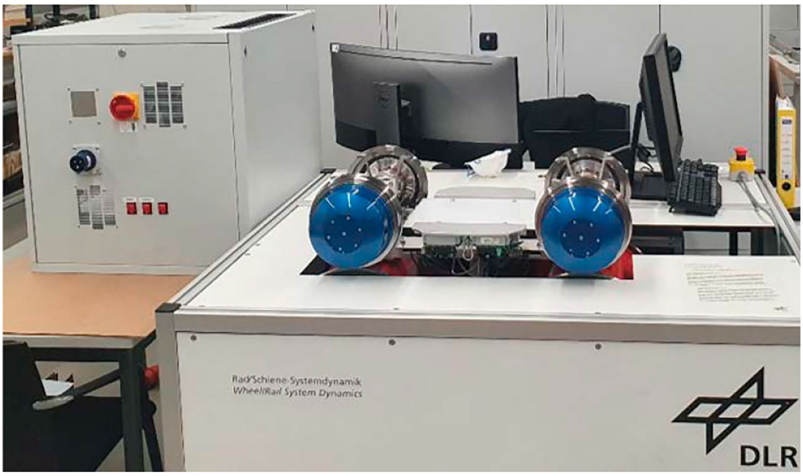

Figure 5. Image of the 1:5 test rig.

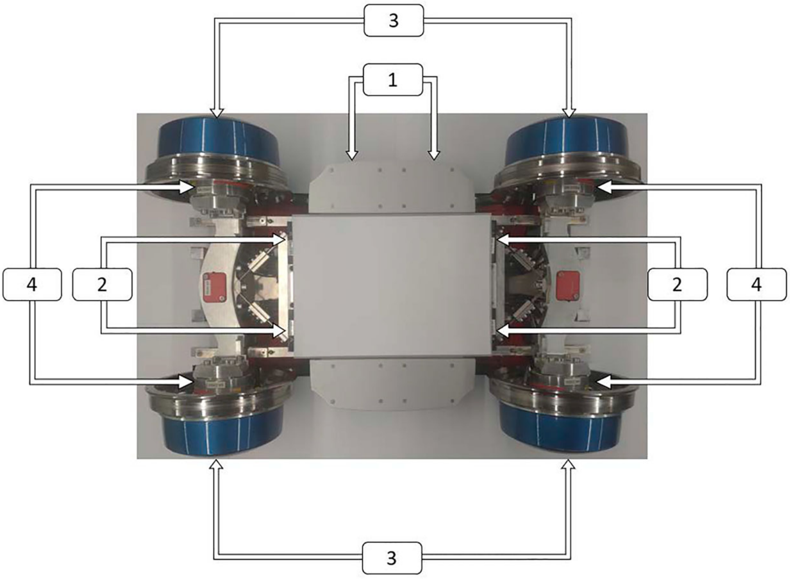

Figure 6. Actuator and Sensors of the test rig, (1) laser sensors for measuring the lateral displacement (2) Laser sensors for calculating the yaw angle (3) Encoders for measuring the angular velocity (4) Force torque sensors to quantify external disturbances.

to the front/rear wheel carrier allowing to calculate the angle between frame and front/rear wheel carrier $\psi_\mathrm{f}/\psi_\mathrm{r}$. The angular velocity of the front left, front right, rear left and rear right wheel is measured using encoders mounted inside the wheels at (3). These allow to calculate the differential angular velocities $\Delta\omega_\mathrm{f}$, $\Delta\omega_\mathrm{r}$. Finally, at (4) each axle bridge is equipped with force-torque sensors mounted on the left and right side, yielding force torque signals along the x, y, z-axis denoted by F_{ijk},M_{ijk} where $i \in \{x, y, z\}$, $j \in \{\mathrm{f}, \mathrm{r}\}$ and $k \in \{\mathrm{l}, \mathrm{r}\}$. The running gear hardware is connected to a rapid control prototyping environment. Simulation models are implemented in MATLAB/Simulink and compiled using the Simulink Real-Time toolbox and a sampling time of $h = 0.005$ s. For a more detailed description of the test rig and its technical details, confer also [6,17].

7.2. Performance

In this scenario, the performance of the combined controller and observer is evaluated. In order to do so, a reference y_ref is given which consists of three steps at 20, 40 and 60 s and is piecewise constant at 0 mm, 1 mm, −2 mm and 0 mm. Three experiments are carried out at a moderate speed of $1\,\mathrm{m\,s^{-1}}$. In the first, the control law (4) is directly applied without an observer as in this laboratory environment the lateral displacement can be measured via the laser sensors. This shall serve as a benchmark to asses which effects stem from the system and the choice of the controller and which from the observer. Secondly, the estimate obtained via the proposed observer defined by Equations (6), (7) and (9) is used with the control law (10) to track the reference. Finally, for comparison, an alternative observer method – the classic Kalman filter [21] – is also applied. It's implementation is standard based on the solution of a continuous Ricatti equation. The main challenge

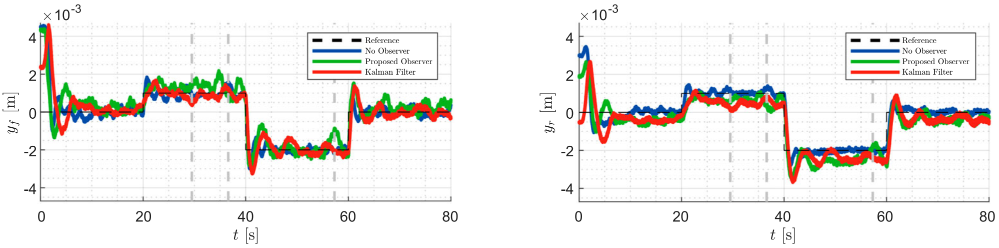

Figure 7. Lateral Displacement.

poses, compared to the proposed observer, the tuning of the covariance matrices. The output covariance matrix R is based on steady state noise while the process covariance matrix Q is tuned based on simulations and hand tuned on the hardware to obtain satisfying results. The chosen covariance matrices are $Q_\mathrm{f} = Q_\mathrm{r} = \mathrm{diag}(2 \cdot 10^{-3}, 1 \cdot 10^{-7}, 8 \cdot 10^{-3})^2$ and $R = \mathrm{diag}(10^{-5}, 0.02)^2)$

The lateral displacement for all three experiments can be seen in Figure 7. It can be seen that in all three experiments the reference is very well tracked. For the front wheel carrier it can be seen that for the experiment without observer and the proposed observer the start of the transition phase and thus the rising time is almost identical at around 0.3 s. For the Kalman Filter the rising time is slightly higher with around 0.6 s. However, for both cases the overshoot of the control with observer is much higher compared to the one without observer. Based on the third step, the overshoot of the experiment without observer is around 35% while for the experiment with the proposed observer as well as the Kalman Filter is around 75%. However, the settling time for all three experiments is around the same for all three steps with around 2 s based on the third step. Note however, that during the steady state oscillations with high amplitudes exist. For the experiment without observer the steady state oscillations of around 0.45 mm while for the experiments with observer these deviations are higher. However, for both designs the deviation is around 0.7 mm. A Fourier transform shows that despite a wide spectrum of frequencies below 0.9 Hz, the other main frequencies are occuring at 1.61, 44.1 and 67.7 Hz, where 1.61 Hz is also the frequency of the wheels rotation for $1\ \mathrm{m\,s^{-1}}$ which is more present when the observer is used. A more detailed analysis on the frequency of the wheels rotation is carried out in Section 7.4. The higher frequencies most likely originate from structural resonances of the test rig. Note that in all three experiments disturbances with unknown origin occasionally lead at instances to a high tracking errors. A sample for each experiment is indicated by a grey vertical line. For the experiment without observer the main deviation can be seen at around 35 s. Here, the tracking error doubles compared to the preceding 6 s, when it stayed below 0.3 mm. A very similar behaviour is very prominent for the experiment with the proposed observer at 57 s and for the experiment with the Kalman Filter at around 30 s.

For the rear wheel carrier the qualitative same behaviour can be seen but with in general smaller tracking errors. The rising time being around 0.75, 0.95 and 1.1 s for the three experiments and overshoot of around 30%, 35% and 40% for the three experiments, respectively. The settling time for the first experiment is around 2 s as well while for the second and third experiment the settling time varies between 5 and 10 s throughout the three steps. Compared to the front axis for which the mean value appeared to be very close to the constant tracking value in both experiments, the rear axis shows this behaviour only for the

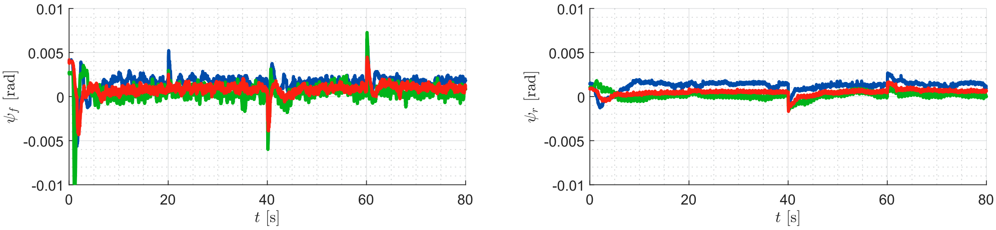

Figure 8. Relative Yaw angle.

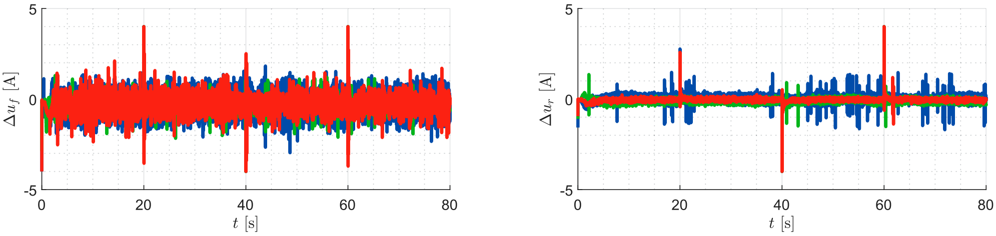

Figure 9. Input variable, differential current.

first experiment without observer. With the proposed observer, the steady-state error is approximately 0.4 mm. The Kalman filter shows a similar steady-state error, differing by only a few hundredths of a millimeter.

The steady state oscillations have a similar spectrum as for the front wheel carrier but smaller deviations of 0.3 and 0.4 mm based on the third step. The same influence of disturbances as for the front wheel carrier can also be observed for the rear wheel carrier but with smaller errors.

All in all it can be seen that the combined observer and controller schemes show similar behaviour to when the lateral displacement would be directly measured with slightly higher errors but overall good tracking performance and smaller errors at rear compared to front. The proposed observer and the Kalman Filter perform similarly well, with both their transient response and steady-state behaviour showing comparable results.

Figure 8 shows the relative yaw angle between frame and wheel carrier. For all three experiments and for front and rear wheel carrier it can be seen that the main action can be seen at the points of time of the step when there is a distinct peak of the relative yaw angle. As before, the overall oscillations are smaller for the rear wheel carrier and the frequency of the wheels 1.61 Hz is extremely prominent when the observer is used but not so when the direct measurement is utilised.

Figure 9 shows the control variable of the front and rear wheel carrier. The qualitative behaviour is very similar to that of the yaw angle with distinct high values at the step times. Notably, the actual signal contains oscillations with very high amplitude compared to the measurements of the lateral displacement and relative yaw angle. Most notably, these oscillations are damped when the observer is used as its intrinsic filtering behaviour smoothes the estimation signal. As expected from the two signals discussed beforehand, the rear wheel carrier requires overall smaller control action compared to the front wheel carrier.

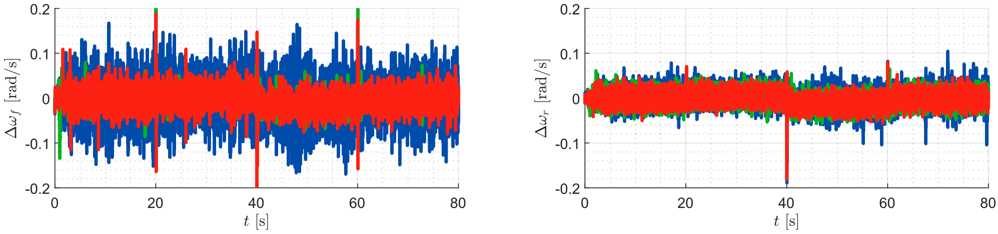

Figure 10. Differential angular velocity.

Finally, Figure 10 shows the differential angular velocity. As shown in Sections 4 and 5, this signal is not used in the controller (4) but the observer (6) relies heavily on it as this is the main quantity allowing to reconstruct the lateral displacement. It can be seen that the signal to noise ratio is very small leading to the fact that the actual signal showing the influence of y is difficult to spot and can usually only be observed using heavy filtering as illustrated in [17]. Interestingly, the oscillations of the first experiment without observer are more prominent than with the observers which is unexpected due to the higher oscillations of the lateral displacement and yaw angle, suggesting unmodelled dynamics for $\Delta\omega$. This, however, holds only for the front wheel carrier, for the rear wheel carrier the signals of both experiments have a very similar noise ratio.

All in all, despite the very noisy angular velocity signals the proposed control scheme using the observer shows satisfying tracking performance.

7.3. *Robustness*

In the second scenario the robustness of the combined observer and controller scheme is evaluated. This is done in a similar manner as in [17]. At 10 and 20 s, a quick but large torque is applied to the front left wheel simulating the effects of rail irregularities. At 30 and 40 s a similar torque is applied to the rear left wheel. Between 50 and 60 s a constant force is applied to the middle of the vehicle simulating the effect of side wind. The measured force and torque of the front and left right sensor is displayed in Figure 11. In Figure 12 the lateral displacement is shown. It is observed that during the rapid perturbations, the lateral displacement changes significantly within a few seconds but returns to the normal steady state within approximately 3 s. Naturally, higher perturbation forces lead to larger induced lateral displacements, though they still converge back to the desired steady state within a few seconds. The displacements at the rear after the two perturbations at the rear wheel

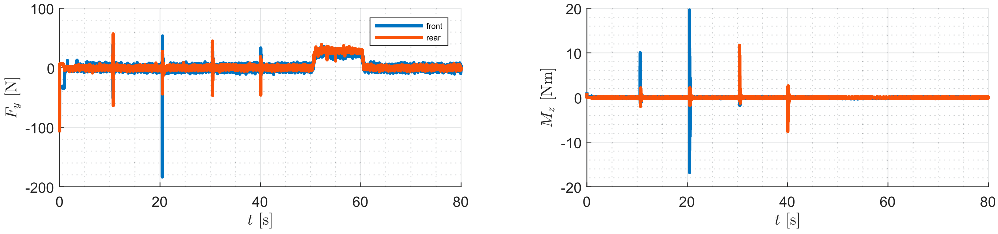

Figure 11. Force Torque measurements.

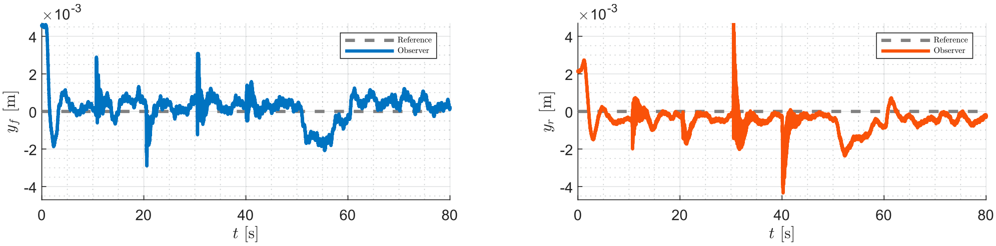

Figure 12. Lateral displacement.

carrier are higher compared to the displacement of the front after the two perturbations at the front despite the front torque being of actual higher magnitude as can be seen in Figure 11. It is also worth mentioning that directly after the perturbation in the transition phase, an oscillation of 39.2 Hz is predominant for both front and rear wheel. However, this oscillation vanishes over time.

For the constant force perturbations, an initial lateral displacement is induced, but the integrator part of the controller generates a corrective force that brings the lateral displacement back to zero. Upon removal of the perturbation, new transient behaviour occurs as the integrator adjusts to the absence of the disturbance. The displacement is of similar magnitude for front and rear axis. Overall, both front and rear wheel carrier show satisfactory robustness with respect to the presented disturbances.

7.4. Vibrations under velocity variance

In Section 7.2, one unexpected phenomenon was the occurrence of steady-state vibrations in the lateral displacement at a frequency corresponding to the vehicle's velocity. More precisely, a Fourier transform revealed a peak at the frequency ω_v, where $\omega_v = \bar{\omega}$ and $\bar{\omega} = \frac{v}{r_0}$, with v being the vehicle velocity and r_0 the wheel radius. To determine whether this effect appears only at $v = 1\,\mathrm{m/s}$ or for all velocities, an experiment was conducted in which the velocity was slowly increased from 0 to 4 m/s within 130 s. During this experiment, a controller was used to keep the lateral displacement at zero. No observer was applied, instead, the direct laser sensor measurements were used. A detailed mathematical investigation of the controller's velocity dependence and its potential adaptation to varying speeds lies beyond the scope of this work and will be explored in future research. Nevertheless, within the limited velocity range of the 1:5 test rig, the proposed controller with constant gains delivered satisfactory performance. The measured lateral displacement at the front and the mean angular velocity of the front wheels were segmented at each sampling time into windows of 5 s and Fourier transformed. The amplitude of each frequency was then plotted as a contour plot in Figure 13. The left-hand side shows the frequencies and amplitudes corresponding to y_f. For better visualisation, three simple reference lines were added that represent multiples of the wheel's angular velocity, which, as stated above, is directly proportional to the vehicle speed. It can first be observed that low frequencies naturally exhibit large Fourier amplitudes. More importantly, the most dominant frequency corresponds directly to the angular velocity of the wheel, forming what can be interpreted as the fundamental frequency. Over the entire range of $\bar{\omega}$, the Fourier transform yields an amplitude at this fundamental frequency that reaches the upper limit of the plotted threshold.

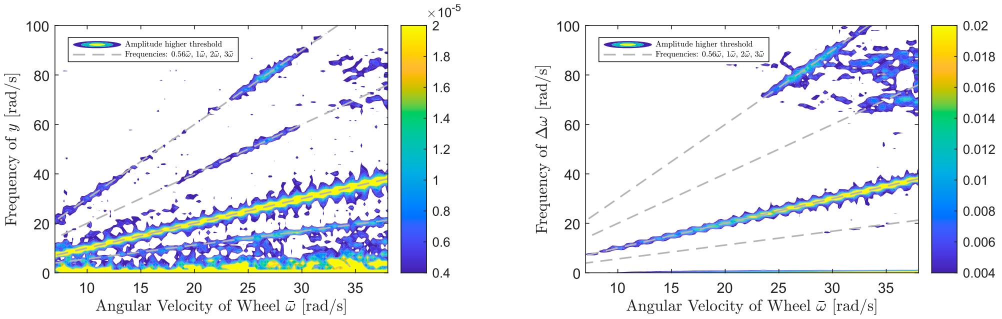

Figure 13. Vibrations.

The second-largest amplitude appears at $0.56\,\bar{\omega}$, which represents a subharmonic component. Additional peaks are visible at $2\,\bar{\omega}$ and $3\,\bar{\omega}$, which correspond to harmonics of the wheel-induced excitation. While the occurrence of such harmonics and conventional subharmonics (e.g. at $\frac{1}{2}\bar{\omega}$ or $\frac{1}{3}\bar{\omega}$) is common, the appearance of a pronounced peak at $0.56\,\bar{\omega}$ is unexpected and its cause is currently unknown. Finally, note that for clarity we have omitted the higher frequencies, which, as mentioned in Section 7.2, correspond to the constant frequencies at 277 and 425 rad s^{-1} arising from structural resonances.

For the angular velocity a very similar image can be seen but with higher harmonics mostly been visible at higher velocities. The fundamental frequency is, however, very prominent for all velocities, explaining why the additional usage of an observer amplifies the occurrence in y as well in the closed loop.

8. Conclusion

This paper presented a comprehensive study on the modelling, control, and state observation for railway running gears with driven independently rotating wheels (DIRWs). The mathematical model of the system was developed with a particular focus on capturing the coupling effects between the front and rear axes, as well as considering angular velocity as an output instead of a state variable. Key details of the model were highlighted to underline the unique challenges posed by the coupled dynamics.

A combined control and observer framework was designed to address these challenges. The control strategy and observer were analytically derived, with a detailed mathematical formulation of the closed-loop system, demonstrating a rigorous approach to ensuring stability and performance. Gain tuning was performed based on decoupled axes, and subsequent validation on the coupled system confirmed that the designed framework performed robustly. Notably, eigenvalue comparisons revealed that the system's dynamic characteristics remained within a similar range, independent of coupling and whether the observer was employed.

Experimental validation with the proposed scheme as well as with a Kalman Filter for comparison purposes was conducted on the 1:5 scaled test rig developed by the German Aerospace Center (DLR). Results demonstrated satisfactory performance, with the lateral reference trajectory being closely followed within a few seconds. While minor oscillations were observed in the steady state, primarily at frequencies linked to the wheel rotation speed, the deviations remained small – within a range of less than 0.5 mm. The front axis exhibited slightly higher deviations compared to the rear axis, which is consistent with its inherently unstable behaviour in the absence of control.

Overall, this study highlights the effectiveness of the proposed combined control and observer approach, offering a robust solution for achieving precise lateral displacement control in DIRWs. Future work will include further refinements to mitigate steady-state oscillations and extend the framework to additional operational scenarios. Furthermore, the full-scale 1:1 prototype currently being commissioned at DLR will enable an even more realistic validation of the proposed algorithms under real-world conditions.

Disclosure statement

No potential conflict of interest was reported by the author.

References

[1] Baeza L, Carballeira J, Roda A, et al. Method for obtaining the modal properties of articulated trains equipped with independently rotating wheels. Veh Syst Dyn. 2006;44:841–854. doi: 10.1080/00423110600643700

[2] Suda Y, Michitsuji Y. Improved curving performance using unconventional wheelset guidance design and wheel-rail interface–present and future solutions. Veh Syst Dyn. 2023;61:1881–1915. doi: 10.1080/00423114.2023.2199937

[3] Kurzeck B, Valente L. A novel mechatronic running gear: concept, simulation and scaled roller rig testing. Lille, France: World Congress on Railway Research; 2011.

[4] Jaschinski A. On the application of similarity laws to a scaled railway bogie model. 1991.

[5] Kurzeck B, Heckmann A, Wesseler C, et al. Mechatronic track guidance on disturbed track: the trade-off between actuator performance and wheel wear. Veh Syst Dyn. 2014;52:109–124. doi: 10.1080/00423114.2014.881514

[6] Keck A, Schwarz C, Meurer T Estimating the wheel lateral position of a mechatronic railway running gear with nonlinear wheel–rail geometry. Mechatronics. 2020;73:102457.

[7] Ji Y, Ren L, Zhou J. Boundary conditions of active steering control of independent rotating wheelset based on hub motor and wheel rotating speed difference feedback. Veh Syst Dyn. 2018;56:1883–1898. doi: 10.1080/00423114.2018.1437273

[8] Perez J, Busturia JM, Mei TX, et al. Combined active steering and traction for mechatronic bogie vehicles with independently rotating wheels. Annu Rev Control. 2004;28:207–217. doi: 10.1016/j.arcontrol.2004.02.004

[9] Liu X, Goodall R, Iwnicki S. Active control of independently-rotating wheels with gyroscopes and tachometers–simple solutions for perfect curving and high stability performance. Veh Syst Dyn. 2021;59:1719–1734. doi: 10.1080/00423114.2020.1780455

[10] Ahn H, Lee H, Go S, et al. Control of the lateral displacement restoring force of IRWs for sharp curved driving. J. Electr Eng Technol. 2016;11:1042–1048. doi: 10.5370/JEET.2016.11.4.1042

[11] Mei TX, Goodall RM. Robust control for independently rotating wheelsets on a railway vehicle using practical sensors. IEEE Trans Control Syst Technol. 2001;9:599–607. doi: 10.1109/87.930970

[12] Yang Z, Lu Z, Sun X, et al. Robust LPV-H_∞ control for active steering of tram with independently rotating wheels. Adv Mech Eng. 2022;14:16878132221130574.

[13] Ewering J, Schwarz C, Ehlers S Integrated model predictive control of high-speed railway running gears with driven independently rotating wheels. IEEE Trans Veh Technol. 2024;73(6):7852–7865.

[14] Wei J, Lu Z, Yin Z Multiagent reinforcement learning for active guidance control of railway vehicles with independently rotating wheels. Appl Sci. 2024;14:1677–1698. doi: 10.3390/app14041677

[15] Posielek T, Heckmann A. Observer design based on steady state and reduced model information with application to running gears with independently rotating driven wheels. Crete, Chania In: Mediterranean Conference on Control and Automation. IEEE; 2024. p. 602–609.

[16] Posielek T. Observer based control for railway vehicleswith independently rotating driven wheels – Front-rear comparison on a 1:5 scale test rig. In: IAVSD International Symposium on Dynamics of Vehicles on Roads and Tracks [accepted]. Shanghai; 2025.

[17] Posielek T. Modelling, system identification and control of a railway running gear with independently rotating wheels on a scaled test rig. 2024.

[18] Heckmann A, Keck A, Kaiser I, et al. The foundation of the DLR railwaydynamics library: the wheel-rail-contact. In: International Modelica Conference. Lund; 2014. p. 465–475.

[19] Lu Z, Wei J, Wang Z Active steering controller for driven independently rotating wheelset vehicles based on deep reinforcement learning. Processes. 2023;11:2677–3002. doi: 10.3390/pr11092677

[20] Posielek T. Observability studies for spacecraft attitude determination based on temperature data [dissertation]. TU Ilmenau; 2022.

[21] Kalman RE. A new approach to linear filtering and prediction problems. 1960.